A galloping energy harvester with flow attachment <img> F

S. Tucker Harvey (ID), I. A. Khovanov (ID), and P. Denissenko (ID)

COLLECTIONS

F This paper was selected as Featured

View Online   Export Citation   CrossMark

ARTICLES YOU MAY BE INTERESTED IN

Superconducting proximity effect in epitaxial Al-InAs heterostructures
Applied Physics Letters 114, 103104 (2019); https://doi.org/10.1063/1.5067363

Quasi-phase-matched second harmonic generation of UV light using AIN waveguides
Applied Physics Letters 114, 103504 (2019); https://doi.org/10.1063/1.5087058

Combined frequency and time domain measurements on injection-locked, constriction-based spin Hall nano-oscillators
Applied Physics Letters 114, 102403 (2019); https://doi.org/10.1063/1.5082692

A galloping energy harvester with flow attachment SCI F

S. Tucker Harvey,[a)] iD I. A. Khovanov, iD and P. Denissenko iD

AFFILIATIONS

School of Engineering, University of Warwick, Coventry CV4 7AL, United Kingdom

[a)]Electronic mail: s.w.tucker-harvey@warwick.ac.uk

ABSTRACT

Aeroelastic energy harvesters are a promising technology for powering wireless sensors and microelectromechanical systems. In this letter, we present a harvester inspired by the trembling of aspen leaves in barely noticeable winds. The galloping energy harvester, a curved blade oriented perpendicular to the flow, is capable of producing self-sustained oscillations at uncharacteristically low wind speeds. The dynamics of the harvesting system are studied experimentally and compared to a lumped parameter model. Numerical simulations quantitatively describe the experimentally observed dynamic behaviour. Flow visualisation is performed to investigate the patterns generated by the device. Dissimilar to many other galloping harvester designs, the flow is found to be attached at the rear surface of the blade when the blade is close to its zero displacement position, hence acting more closely to aerofoils rather than to conventionally used bluff bodies. Simulations of the device combined with a piezoelectric harvesting mechanism predict higher power output than that of a device with the square prism.

The development of energy harvesters for wireless sensors is an area that has received significant interest in recent years due to their potential for low maintenance and low cost energy solutions.[1–7] The galloping instability of prismatic sections, which can result in the formation of self-sustained oscillations under incident flow conditions,[8,9] can be exploited for the harvesting of wind energy. This is typically achieved by the mounting of a prismatic section to the end of a cantilever beam with a transduction mechanism.[10–15] The design of the tip geometry is a critical factor in determining the nature of the fluid-structure interaction and hence the performance of a galloping energy harvester.

Investigating the influence of different tip cross-section geometries on the performance of galloping energy harvesters has been the subject of several studies with focus being placed on the square, isosceles triangular, and the D shaped cross sections.[16–19] Mathematical approaches have been formulated with both lumped parameter and coupled non-linear distributed models,[10,17] while experimental comparisons have also been performed with flow conditions controlled inside a wind tunnel.[16]

The nature of the flow field around the tip geometry of a galloping energy harvester fundamentally determines the potential efficiency of the device. The flow around a galloping square cross section has been examined by both numerical and experimental means.[20] The mechanism by which galloping oscillations are formed has been shown to relate to the separation and reattachment of the flow on the sides of the square section, while the flow on the rear face remains detached.[20] Similarly, in the case of the isosceles triangular cross section, the boundary layer has been demonstrated to be detached on at least one face depending on the angle of attack.[21,22] The flow around a D shaped cross section has been studied numerically with regard to semicircular aerofoils and also shown to be detached at low angles of attack.[23,24] Hence, the mechanisms for galloping oscillations for the square, isosceles triangular, and D-shaped sections have been shown to relate to detached flows.

In this letter, an alternative tip geometry is presented for a galloping energy harvester, initially inspired by the trembling of aspen leaves at low wind speeds. The curved blade geometry is closer to an aerofoil, rather than a bluff body, which has typically been studied. The flow around the geometry is observed to be fully attached when oscillations are large and the blade is close to its zero displacement position, and galloping oscillations are observed at flow velocities of less than $1\,\mathrm{ms}^{-1}$ with a prototype device. The time-dependent flow around the blade is studied by smoke wire visualisation and Particle Image Velocimetry (PIV),

TABLE I. System parameters.

Parameter	Symbol	Value (unit)
Blade base circle radius	R	75 (mm)
Blade half arc angle	γ	45°
Blade chord length	Ch	75 (mm)
Blade thickness	t	10 (mm)
Blade span	S	75 (mm)
Beam length	l_b	150 (mm)
Beam width	w_b	12.5 (mm)
Beam thickness	t_b	0.5 (mm)

and the dynamics of the harvester are investigated by both wind tunnel testing and mathematical modelling.

The harvester consisted of a cantilever beam and a curved blade. The section of the curved blade was chosen to be a circular arc, and the cantilever beam was of steel construction. Further details of the system parameters are presented in Table I. The blade was rigidly mounted to the end of the beam and the beam was mounted within a low speed wind tunnel such that the blade was oriented perpendicular to the flow direction. The wind tunnel had a test section of 1.04×1.37 m with a turbulence intensity of less than 1% and was capable of obtaining stable flow velocities between 0.5 ms^{-1} and 24 ms^{-1}. The observed oscillations relate to the motion of the blade in a plane normal to the flow direction as illustrated in Fig. 1. Oscillations were experimentally observed with flow velocities ranging from 0.9 ms^{-1} to 5.8 ms^{-1}, corresponding to Reynolds numbers of 6.2×10^3 and 4.0×10^4.

To investigate the flow structures around the blade, flow visualisation was performed with a hot wire smoke generator and a laser sheet curved along the blade trajectory. Images were captured by a Phantom high speed camera mounted above the harvester at 1000 fps with an image size of 1152×720 pixels. The analysis was performed with Dantec PIV software using an adaptive correlation algorithm. Figure 2 demonstrates the configuration of the PIV and motion tracking systems within the test section.

Figure 3 illustrates the flow visualisation and PIV results for steady state oscillations at two different reduced
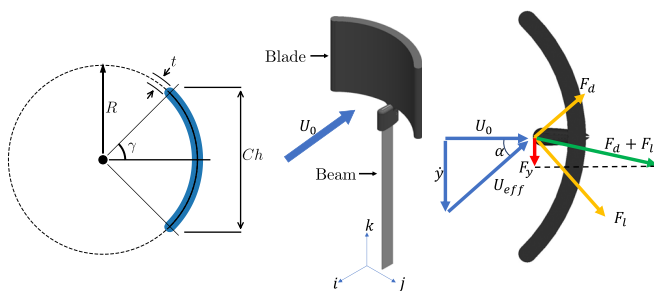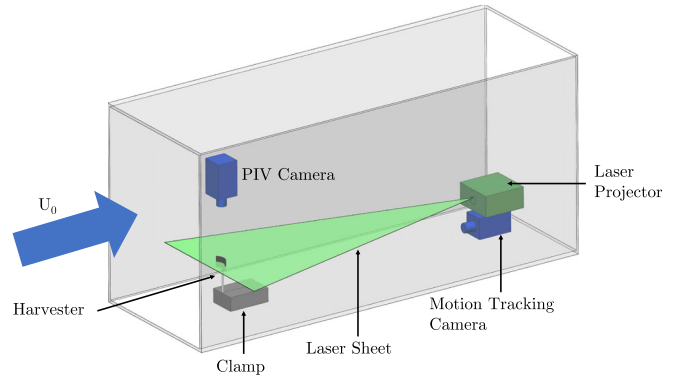

FIG. 2. Illustration of the low speed wind tunnel experimental setup.

velocities. Reduced velocity U* is defined as $\frac{U_0}{f_n Ch}$, where f_n is the natural frequency of the harvester and U_0 represents the freestream flow velocity. The blade is viewed from above with the rear surface facing the bottom of the image. The blade position is close to that of maximum velocity, and the velocity field is plotted in a frame of reference moving with the blade. The visualisation reveals leading edge separation and a large
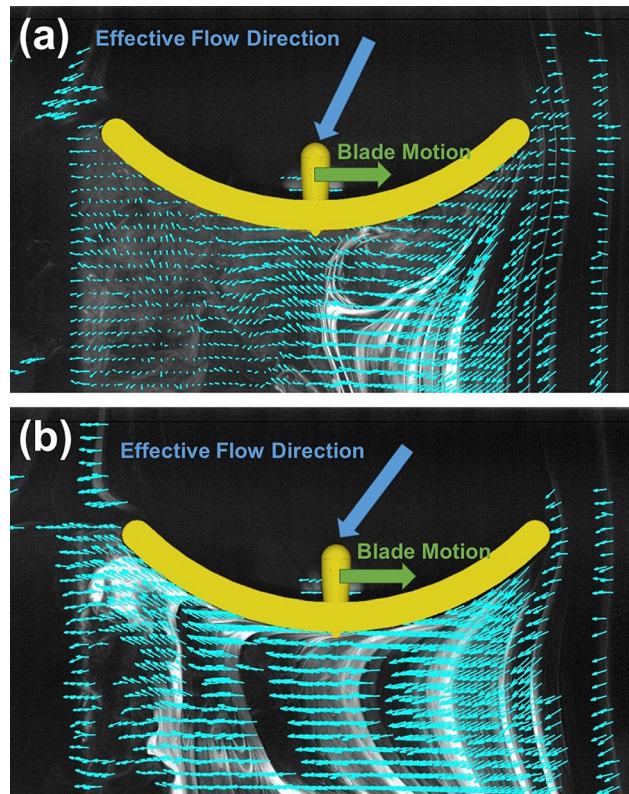

FIG. 3. Flow visualisation results at the mid-position, where the tip speed is maximum. Case (a): the flow velocity is 1.13 ms^{-1}, the reduced velocity is $U^* = 5.0$, and the angle of attack is $\alpha = 26°$. Flow detachment and the turbulent wake are observed. Case (b): the flow velocity is 1.37 ms^{-1}, the reduced velocity is $U^* = 6.0$, and the angle of attack is $\alpha = 37°$. Attached flow is observed.

FIG. 1. Illustration of geometry and definition of variables. Oscillations result in motion in the j, k plane. U_0 denotes the freestream flow velocity, $\dot{y}$ is the linear velocity of the blade centre of mass, U_{eff} is the effective flow velocity, and α is the effective angle of attack. F_l and F_d denote the lift and drag forces, respectively, while F_y is the aerodynamic force in the y direction.

wake at low angle of attack; however, at higher angles of attack, the flow is found to become attached. During each half-oscillation cycle, the flow becomes detached as the blade stops at maximum displacement. As the blade then acceler-ates back to its mid-position, the angle of attack increases and the flow becomes attached. Pronounced unsteady flow effects were observed with flow patterns varying substan-tially between oscillation cycles. Wake interaction was observed at the lowest flow velocity with shed vortices being convected back onto the rear surface of the blade as the direction of motion reversed.

The dynamics of the harvester were captured with a 2D motion tracking system based on a camera with a 1920×1080 pixel resolution and a frame rate of 50 fps. The position of the motion tracking camera within the test section is demonstrated in Fig. 2. Three fluorescent markers were tracked, allowing the calculation of the position of the centre of mass of the blade. The dynamics of the system could then be described by the dis-placement of the blade centre of mass along the j axis in Fig. 1. The precision of the system was estimated by tracking a station-ary blade, resulting in a standard deviation of 0.24 mm or $2.2 \times 10^{-4}Ch$ over a 1-min time series. The trajectories of the blade centre of mass are illustrated in Fig. 4 in the state space.

The harvester exhibited a subcritical Hopf bifurcation in the wind tunnel experiment, with oscillations beginning at the flow velocity of 1.11 ms^{-1} while the flow velocity was increased and remaining until the flow velocity of 0.90 ms^{-1} when flow velocity was decreased as shown by the blue line in the Fig. 5 inset. The Strouhal number was determined experimentally behind a static blade to be 0.2. As the Hopf bifurcation occurs close to a reduced velocity of $1/St$, unsteady effects are likely to have a significant influence on the onset of oscillations. The maximum measured velocity amplitude of the blade occurred at the oscillation amplitude of 0.24 m or $2.2Ch$. A branch of smaller amplitude oscillations was found to exist at wind speeds above 3.1 ms^{-1}, which we attribute to a regime when the flow is always detached from the back of the blade. The amplitude variation of the limit cycles was evaluated by computing the standard devia-tion of the peaks in y displacement. Normalising with the y dis-placement RMS, a maximum normalised amplitude variation of 1.2% is obtained occurring at the smallest amplitude cycle in the subcritical branch.
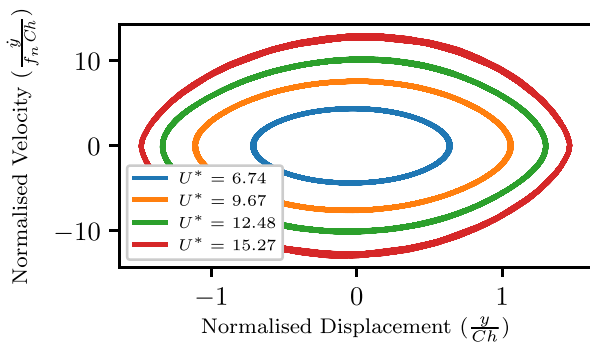

FIG. 4. Nondimensional state space trajectories obtained with the curved blade (experimental).
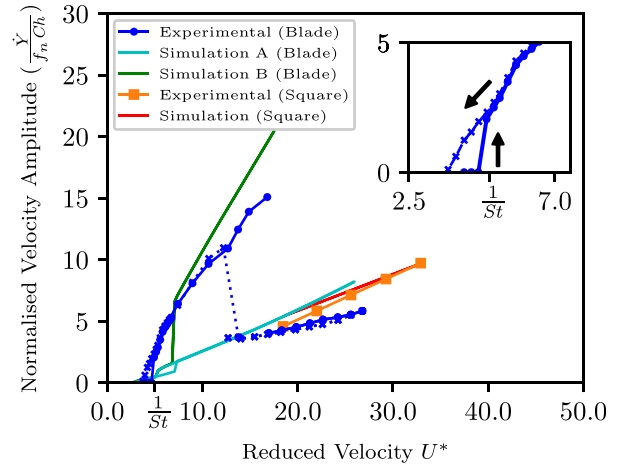

FIG. 5. Normalised blade velocity amplitude with reduced velocity. Dotted lines with crosses represent behaviour with decreasing reduced velocity. The reduced velocity of $\frac{1}{St}$ is marked.

Similar to Barreo-Gil,[10] by considering small deflections of the beam, the position of the system can be reduced to a linear displacement in the y direction. This allows the system to be described by a second order ordinary differential equation

$$\ddot{y} = \frac{1}{m_{tip}} \left(F_y(\dot{y}) - K_{beam}y - C_{damp}\dot{y} \right), \tag{1}$$

where m_{tip}, K_{beam}, and C_{damp} denote the tip mass, beam stiffness, and damping coefficient, respectively. The aerodynamic force $F_y(\dot{y})$ could be represented as a function of the non-dimensional force coefficient C_y by

$$F_y = \frac{1}{2}\rho A_f C_y(\alpha)\left(U_0^2 + \dot{y}^2\right), \tag{2}$$

where ρ is the density of air, A_f is the frontal area, and U_0 is the flow velocity. The aerodynamic force coefficient C_y can be writ-ten in terms of the lift and drag coefficients, C_l and C_d, as

$$C_y = C_l \cos(\alpha) - C_d \sin(\alpha), \tag{3}$$

where α is the effective angle of attack of the blade, which is given by $\alpha = \arctan(\dot{y}/U_0)$, as illustrated in Fig. 1. The lift and drag coefficients of a static blade were measured experimentally with a force balance, and the resulting coefficients were used to calculate C_y with Eq. (3). These statically measured force coeffi-cients are demonstrated in Fig. 6. The numerical simulation of Eq. (1) could then be performed by linearly interpolating the C_y coefficient from the statically measured coefficients at each time step.

Further to the aerodynamic force coefficient C_y, compari-son of experimental bifurcation curves to the mathematical model (1) also required the beam stiffness K_{beam} and beam mechanical damping C_{damp} to be evaluated. K_{beam} was found by matching the experimental natural frequency, and C_{damp} was determined by exponential fitting of decaying oscillations at zero wind velocity.
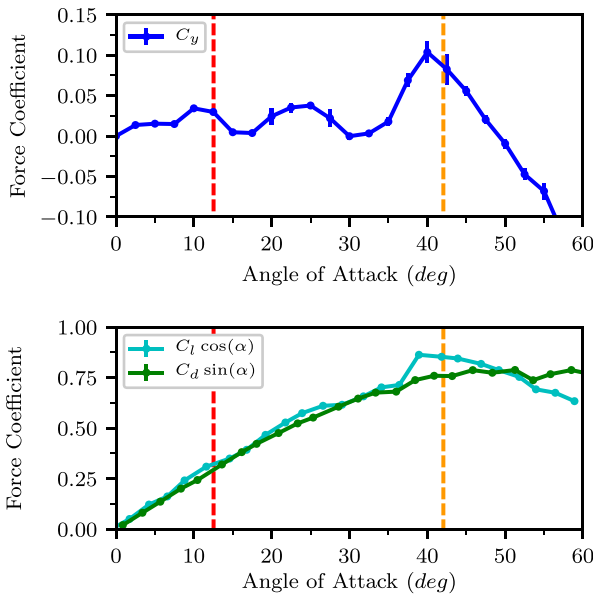
FIG. 6. Curved blade statically measured force coefficients. C_y calculated by Eq. (3). Dashed lines represent the mean of the highest four experimental angles of attack on each branch, also shown in Fig. 7.

The mathematical model was simulated with the use of two different cases of initial conditions. Simulation A relates to the case in which the initial conditions started with a small perturbation and then, once limit cycles began to form, the end conditions of each simulation were used as the initial conditions of the following while flow velocity was increased. This provided continuation of cycles in the state space. The initial conditions of simulation B were set consistently to relate to an angle of attack of $55°$. This allowed higher amplitude branches to be evaluated. A comparison of the experimental dynamics and mathematical model in terms of blade velocity amplitude is presented in Fig. 5.

The mathematical model also demonstrates two branches of stable limit cycles, occurring at similar velocity amplitudes to the experimentally measured cycles. In agreement with experimental data, the Hopf bifurcation was subcritical in the model, although the subcritical branch was of significantly shorter length. The bifurcations however differed with the low amplitude branch growing from the Hopf bifurcation in the model, rather than the high amplitude branch as observed in the wind tunnel experiment. The simulation results also demonstrate an additional hysteresis loop formed by a pair of saddle node bifurcations, occurring just after the Hopf bifurcation. In Fig. 6, this relates to the harvester moving from operation around the first C_y peak to the second C_y peak as flow velocity is increased. Unsteady flow effects may hence allow the oscillations to surpass the second C_y peak in the experiment moving directly to the large amplitude branch. Experimental results obtained with a square prism geometry with equal A_f and mounted onto the same beam are also presented in Fig. 5 and compared to simulations using the polynomial representation of C_y with the coefficients determined by Parkinson.[8]

The maximum angle of attack α for both the experimental dynamics and the mathematical model is demonstrated in Fig. 7. In both the experimental dynamics and mathematical model, the maximum angle of attack can be seen to become insensitive to the flow velocity far from the Hopf bifurcation. The angles of attack to which the low and high amplitude branches are tending towards can be seen to correspond to the first and last peaks in C_y in Fig. 6. This is illustrated by the dashed lines in Figs. 7 and 6. The last peak in C_y in Fig. 6 can be seen to relate to the sudden jump in the projection of the lift coefficient, $C_l \cos \alpha$. This is caused by the transition to attached flow at around $37.5°$, which corresponds closely to the visualisation of attached flow in Fig. 3(b). Hence, the high amplitude branch can be attributed to the attachment of the flow on the rear surface of the blade.

To investigate the energy harvesting potential of the curved blade, an additional equation was simulated representing a piezoelectric harvesting circuit given by

$$\dot{V} = -\frac{1}{C_p}\left(\frac{V}{R_l} + \theta \dot{y}\right), \tag{4}$$

where C_p is the capacitance of the piezoelectric element, R_l denotes the load resistance, V is the generated voltage, and θ is the electromechanical coupling factor. An additional term $\frac{\theta V}{m_{tip}}$ is also added to Eq. (1) to provide the feedback from the piezoelectric. Typical values for θ and C_p were taken from the work of Alhadidi[25] by matching the nondimensional coupling factor $\frac{\theta^2}{C_p m_{tip} f_n^2}$. By simulating the system with the additional equation, the potential power output could be predicted. For comparison, simulations were also performed with the polynomial representation of C_y for the square prism developed by Parkinson.[8] The load resistances were optimised to maximised output power. The results for both the curve blade and square prism are shown in Fig. 8. When operating in the higher amplitude branch, the curved blade is predicted to produce significantly more power than the square prism. Hence, the attachment of the flow on the rear surface of the blade results in a larger projected lift
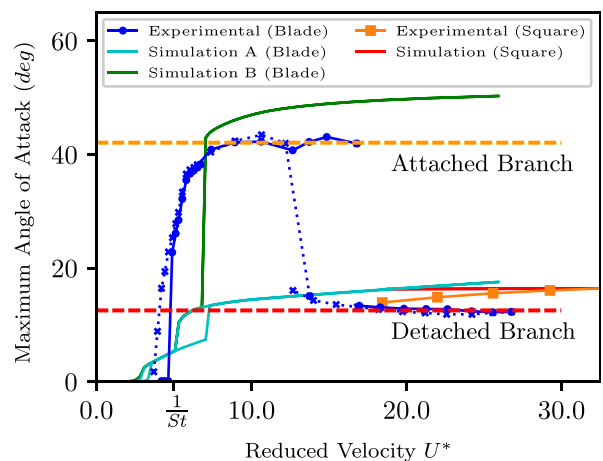

FIG. 7. Maximum angle of attack versus reduced velocity. Dotted lines with crosses represent the branch with decreasing flow velocity. Dashed lines represent the mean of the four highest velocity points on each branch.
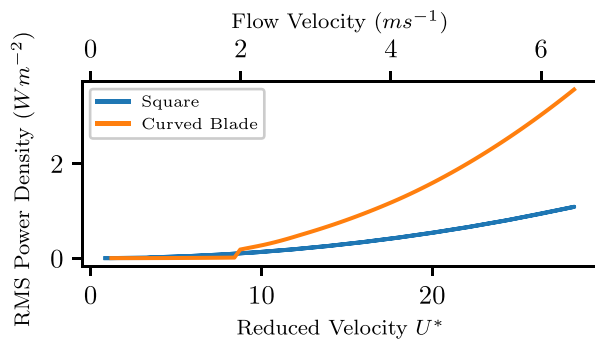
FIG. 8. Simulated output power with the additional harvesting circuit equation (Eq. 4).

coefficient $C_l \cos \alpha$, which leads to a peak in C_y as demonstrated in Fig. 6 at around 40° angle of attack. This leads to the appearance of a higher amplitude limit cycle which simulations have shown to be capable of producing more power than the widely considered square cylinder.

In this letter, we have presented a curved blade geometry for a galloping energy harvester, inspired by the trembling of an aspen leaf. Flow visualisations and PIV measurements have demonstrated that the flow becomes attached to the rear face of the blade when the blade velocity becomes large enough. The blade has hence been shown to act more closely to an aerofoil rather than a bluff body, providing the prospect of greater aerodynamic efficiencies. Experimental investigation of the dynamics has demonstrated the existence of two branches of limit cycles, one attributed to a regime where the flow attaches to the blade and the other where the flow remains detached. A lumped parameter model has been constructed and shown to also exhibit two branches of limit cycles of amplitudes close to those observed experimentally. The discrepancies between the model and the experiment are attributed to the unsteady nature of the flow around the harvester tip which requires further investigation. Simulations have also predicted the curved blade geometry to produce more power than the square prism when operating in the high amplitude branch.

REFERENCES

[1]S. Roundy and P. K. Wright, Smart Mater. Struct. **13**, 1131 (2004).
[2]N. A. Khovanova and I. A. Khovanov, Appl. Phys. Lett. **99**, 144101 (2011).
[3]J. McCarthy, S. Watkins, A. Deivasigamani, and S. John, J. Sound Vib. **361**, 355 (2016).
[4]R. Naseer, H. Dai, A. Abdelkefi, and L. Wang, Appl. Energy **203**, 142 (2017).
[5]F.-R. Liu, H.-X. Zou, W.-M. Zhang, Z.-K. Peng, and G. Meng, Appl. Phys. Lett. **112**, 233903 (2018).
[6]X. He, X. Yang, and S. Jiang, Appl. Phys. Lett. **112**, 033901 (2018).
[7]M. Y. Zakaria, M. Y. Al-Haik, and M. R. Hajj, Appl. Phys. Lett. **107**, 023901 (2015).
[8]G. V. Parkinson and J. D. Smith, Q. J. Mech. Appl. Math. **17**, 225 (1964).
[9]A. B. Rostami and M. Armandei, Renewable Sustainable Energy Rev. **70**, 193 (2017).
[10]A. Barrero-Gil, G. Alonso, and A. Sanz-Andres, J. Sound Vib. **329**, 2873 (2010).
[11]L. Zhao, L. Tang, and Y. Yang, Jpn. J. Appl. Phys., Part 1 **53**, 060302 (2014).
[12]D. Vicente-Ludlam, A. Barrero-Gil, and A. Velazquez, J. Fluids Struct. **51**, 281 (2014).
[13]H. L. Dai, A. Abdelkefi, U. Javed, and L. Wang, Smart Mater. Struct. **24**, 045012 (2015).
[14]P. Hémon, X. Amandolese, and T. Andrianne, J. Fluids Struct. **70**, 390 (2017).
[15]L. Zhao, L. Tang, and Y. Yang, J. Intell. Mater. Syst. Struct. **27**, 453 (2016).
[16]Y. Yang, L. Zhao, and L. Tang, Appl. Phys. Lett. **102**, 064105 (2013).
[17]A. Abdelkefi, Z. Yan, and M. R. Hajj, J. Intell. Mater. Syst. Struct. **25**, 246 (2014).
[18]A. Bibo and M. F. Daqaq, Appl. Phys. Lett. **104**, 023901 (2014).
[19]G. Hu, K. T. Tse, and K. C. S. Kwok, Appl. Phys. Lett. **108**, 123901 (2016).
[20]S. Luo, Y. Chew, and Y. Ng, J. Fluids Struct. **18**, 103 (2003).
[21]J. Tu, D. Zhou, Y. Bao, Z. Han, and R. Li, J. Fluids Struct. **45**, 107 (2014).
[22]B. Seyed-Aghazadeh, D. W. Carlson, and Y. Modarres-Sadeghi, J. Fluid Mech. **817**, 590–618 (2017).
[23]S. A. Isaev, P. A. Baranov, Y. V. Zhukova, E. I. Kalinin, and J. J. Miau, J. Eng. Phys. Thermophys. **89**, 73 (2016).
[24]S. I. Isaev, P. A. Baranov, A. G. Sudakov, and A. E. Usachev, J. Eng. Phys. Thermophys. **89**, 1500 (2016).
[25]A. H. Alhadidi and M. F. Daqaq, Appl. Phys. Lett. **109**, 033904 (2016).